# LOW-COST SURFACE PASSIVATION FOR BLACK SILICON SOLAR CELLS BY LIQUID PHASE DEPOSITION TECHNIQUES

# **SHERIFF MUHIDDIN AHMAD**

UNIVERSITI SAINS MALAYSIA

# LOW-COST SURFACE PASSIVATION FOR BLACK SILICON SOLAR CELLS BY LIQUID PHASE DEPOSITION TECHNIQUES

by

# **SHERIFF MUHIDDIN AHMAD**

Thesis submitted in fulfilment of the requirements for the degree of Doctor of Philosophy

December 2023

### **ACKNOWLEDGEMENT**

In the name of Allah, the Most Beneficent, the Most Merciful.

All praise and thanks are due to the Almighty Allah (S.W.T.), the lord of the universe, for bestowing me with health, capability, strength, wisdom, and knowledge to complete this Ph.D. thesis. ALHAMDULILLAH.

First, I would like to express my deep gratitude and appreciation to my main supervisor, Associate Professor Ts. Dr. Mohd Zamir bin Pakhuruddin, for his tireless support and guidance during the research. My appreciation also goes to my cosupervisor, Professor Dr. Md. Roslan Hashim, for his support, advice, and encouragement. My sincere appreciation and word of thanks to the Nano-Optoelectronics Research and Technology Laboratory (NOR Lab) staffs. I would also like to express my profound gratitude to the Photovoltaics Materials and Devices (PVMD) research members. May Allah (S.W.T) reward them all abundantly. AMIN YA RABBAL`ALAMIN.

Finally, my special thanks and appreciation go to my family, especially my late mum and siblings, for their love, patience, prayers, and encouragement during my research journey. My extreme gratitude goes to the love of my life, my wife (Engr Bintu Tijjani Maina), and my children (Ahmad, Tijjani, Muhammad, Mustapha, Fatima, Kasim, and the twins Abdulrahman and Abdulrazak) for their support, patience, endurance, and prayers through the peaks and valleys of my postgraduate life.

Sheriff Muhiddin Ahmad

Penang, Malaysia, December 2023

## TABLE OF CONTENTS

ACK	NOWL	EDGEMENT	ii
TABI	LE OF	CONTENTS	iii
LIST	OF TA	BLES	vi
LIST	OF FIG	GURES	vii
LIST	OF SY	MBOLS	xiii
LIST	OF AB	BREVIATIONS	xvi
ABST	ΓRAK		XX
ABST	ГRАСТ		xxii
СНА	PTER 1	INTRODUCTION	1
1.1	Introd	uction	1
1.2	Proble	m statement	8
1.3	Object	tives	10
1.4	Thesis	outline	11
СНА	PTER 2	THEORETICAL BACKGROUND AND LITERATURE REVIEW	13
2.1	Introd	uction	13
2.2	Soları	radiation	13
2.3	Silico	n solar cells	14
	2.3.1	Operating principle	17
	2.3.2	Solar cell efficiency parameters	20
2.4	Black	silicon solar cells	23
	2.4.1	Black silicon	26
	2.4.2	Properties of black silicon	27
	2.4.3	Refractive index grading effect	31
	2.4.4	Surface recombination	35
2.5	Fabric	ation of black silicon	36

	2.5.1	Techniques for fabrication of black silicon	37
	2.5.2	Metal-assisted chemical etching (MACE)	38
2.6	Surfac	e passivation	42
	2.6.1	Fundamentals of surface passivation	43
	2.6.2	Surface passivation materials	44
	2.6.3	Surface passivation techniques	50
	2.6.4	Surface passivation parameters	51
2.7	Liquid	phase deposition (LPD)	54
	2.7.1	Fundamentals of LPD process	56
	2.7.2	LPD of silicon dioxide (SiO <sub>2</sub> ) thin film	56
	2.7.3	Effects of hydrofluorosilicic acid (H <sub>2</sub> SiF <sub>6</sub> ) concentration (precursor)	58
	2.7.4	Effects of boric acid (H <sub>3</sub> BO <sub>3</sub> ) concentration	59
	2.7.5	Effects of temperature	60
	2.7.6	Effects of calcination	60
CHAI	PTER 3	METHODOLOGY	62
3.1	Introd	uction	62
3.2	Wafer	preparation	62
3.3	Fabric	ation of black silicon by one-step MACE process	63
3.4	Charac	cterizations of black silicon	65
	3.4.1	Atomic Force Microscope (AFM)	65
	3.4.2	Field Emission Scanning Electron Microscopy (FESEM)	67
	3.4.3	UV-Vis-NIR spectrophotometer	68
3.5	Depos	ition of LPD SiO <sub>2</sub> thin film	70
3.6	Charac	cterizations of LPD SiO <sub>2</sub> thin film	72
	3.6.1	Thickness measurement	72
	3.6.2	Energy Dispersive X-ray Spectroscopy (EDX)	73

	3.6.3	Attenuated total reflectance-Fourier-transform infrared (ATR-FTIR) spectrometer	
3.7	Fabric	ation of black silicon solar cells with LPD of SiO <sub>2</sub> thin film	75
3.8	Chara	cterizations of black silicon solar cells with LPD SiO <sub>2</sub> thin film	ı79
	3.8.1	Hall effect measurement	79
	3.8.2	Current-voltage curve	82
CHA	PTER 4	RESULTS AND DISCUSSIONS	84
4.1	Introd	uction	84
4.2	Black	silicon fabricated by one-step MACE process	84
	4.2.1	Effects of etching time	84
4.3	Depos	ition of SiO <sub>2</sub> thin film by LPD process	91
	4.3.1	Effects of deposition time	91
	4.3.2	Effects of boric acid concentration	99
	4.3.3	Effects of hydrofluorosilicic acid concentration	104
	4.3.4	Effects of deposition temperature	108
4.4	Black	silicon solar cells with LPD SiO <sub>2</sub> thin film	114
	4.4.1	Composition analysis	114
	4.4.2	Surface morphological properties	115
	4.4.3	Optical properties	118
	4.4.4	Electrical properties	119
CHA	PTER 5	CONCLUSIONS AND RECOMMENDATIONS	124
5.1	Concl	usions	124
5.2	Recon	nmendations	125
5.3	Novel	ties	126
REFE	ERENC	ES	128
LIST	OF PU	BLICATIONS	

## LIST OF TABLES

		Page
Table 2.1	Status of MACE-based b-Si literature: synthesis processes, etchant composition, etch time, nanotexture type, nanotexture length, WAR and PCE achieved	30
Table 2.2	State of the literature on solar cells based on LPD-SiO <sub>2</sub> : substrate types, texture types, synthesis types, thickness, refractive index, WAR and PCE attained	61
Table 3.1	Experimental conditions and measurements performed for b-Si fabricated using the one-step MACE process	65
Table 4.1	Properties of b-Si-NW fabricated with one-step MACE at different deposition times.	91
Table 4.2	The RMS roughness of b-Si NWs as a function of the processing time of the LPD process.	96
Table 4.3	WAR of the LPD-SiO <sub>2</sub> thin films within the wavelength range of 300 to 1100 nm on b-Si NWs as a function of H <sub>3</sub> BO <sub>3</sub> concentration.	103
Table 4.4	WAR of the LPD-SiO <sub>2</sub> thin films at the wavelength range from 300 to 1100 nm on b-Si NWs as a function of H <sub>2</sub> SiF <sub>6</sub> concentration.	107
Table 4.5	WAR of the LPD-SiO <sub>2</sub> thin films at the wavelength range from 300 to 1100 nm on b-Si NWs as a function of deposition temperature.	113
Table 4.6	Hall effect results for the samples (c-Si, LPD-SiO <sub>2</sub> c-Si, b-Si NWs and LPD-SiO <sub>2</sub> /b-Si NWs-based solar cells)	119
Table 4.7	J-V characteristics of c-Si and b-Si NWs based solar cells without LPD-SiO <sub>2</sub> film and c-Si and b-Si NWs based solar cells coated with LPD-SiO <sub>2</sub> film	122

## LIST OF FIGURES

		Page
Figure 1.1	Depicts (a) Global electricity generation from renewables and fossil fuels until 2050 and (b) Global installed capacity by energy source (adapted from IRENA's Global Renewables Outlook, 2020) [6].	2
Figure 1.2	World market share for different c-Si solar cell technologies and extrapolation of demand to the Year 2030. Source: ITRPV 2020 [21].	4
Figure 1.3	National Renewable Energy Laboratory (NREL) solar cell efficiency chart [27].	5
Figure 2.1	AM1.5G standard solar spectrum (spectral irradiance as a function of wavelength), direct part of AM0 spectrum of AM1.5G spectrum. The plotted data are available from the original NREL data file [85] and the embedded image (for AM 0, AM 1 and AM 1.5) was taken from the Newport company website [86].	14
Figure 2.2	Two-level system showing photon absorption only at a certain energy level (wavelength) (a-e) with an increasing number of energy levels (horizontal) for direct bandgap material like GaAs. The colour of the arrows represents the colour of the absorbed light, while (f) is the band structure of c-Si (indirect bandgap material). (Taken from [89]).	16
Figure 2.3	Schematic of p-n junction showing the motion of mobile electrons and holes due to diffusion and the "built-in" electric field [88].	17
Figure 2.4	Fermi levels of a) n-doped and p-doped semiconductors alone, b) a p-n homojunction in thermal equilibrium and c) an ideal $n + pp$ + device upon illumination [89]	20
Figure 2.5	Electrical circuit of a solar cell showing generated photon current in parallel with p-n-junction diode and a shunt resistor, and in series with another resistor (a) and current density-voltage characteristic curves of solar cell under illumination and in the dark (b) (adopted from [29]).	20
Figure 2.6	(a) Needle-like shape, (b) pyramid shape, and (c) cylinder shape c-Si structures [93].	24
Figure 2.7	Images of (a) reference c-Si and 80s etched b-Si using one- step MACE process [38]	27

Figure 2.8	Light-trapping b-Si nanotextures fabricated by one-step MACE; Scale bar is 2 μm and 200 nm for the inset (adopted from [47]).	32
Figure 2.9	Light trapping mechanisms in nanotextured [47]	33
Figure 2.10	Schematic representation of the c-Si wafer etching mechanism leading to the formation of a b-Si NW array in an one-step MACE process (adopted from [136])	39
Figure 2.11	The illustrations of the passivation mechanisms: the chemical passivation and the field-effect passivation of the Al <sub>2</sub> O <sub>3</sub> /Si interface [149]	43
Figure 2.12	Schematic diagram of n-type bifacial c-Si solar cell passivated by LPD SiO <sub>2</sub> thin films [160]	44
Figure 2.13	Refractive index of a-SiN <sub>x</sub> : H films vs density of H, Si, and N [162].	47
Figure 2.14	(a, b) Electron and hole density under the Si surface, under the influence of a negative fixed surface charge of $Q_f$ =2×10 <sup>12</sup> cm <sup>-2</sup> (c) band bending under the influence of $Q_f$ for 2 $\Omega$ cm p-type c-Si wafer [198].	52
Figure 2.15	Schematic diagram of the deposition process for LPD-SiO <sub>2</sub> [251].	55
Figure 2.16	A schematic of LPD-SiO <sub>2</sub> film formation. (a) and (b) the Si-F bond reacts with the Si-OH bond to form a Si-O-Si bond and release HF; HF attacks the Si-OH bond and forms a Si-F bond, releases H <sub>2</sub> O, (c) two adjacent Si-OH bonds react with each other to form a Si-O-Si bond[212].	58
Figure 2.17	Effect of supersaturation for homogeneous and heterogeneous nucleation rates [212].	59
Figure 3.1	Diamond Scriber (Model type; RV129) in Nano- Optoelectronics Research and Technology Laboratory (NOR lab) USM.	63
Figure 3.2	Flow chart of fabrication of b-Si NWs	64
Figure 3.3	Image and schematic diagram of Atomic Force Microscope (AFM) (Model: Agilent Cary 5000) [229]	66
Figure 3.4	Image and schematic diagram of working principle of field emission scanning electron microscopy (FESEM) (model: FEI Nova NanoSEM 450) [230].	68

Figure 3.5	Image and schematic diagram of working principle of UV- Vis-NIR spectroscopy (Agilent Carry 5000; schematic is adopted from [231])	69
Figure 3.6	Flow chart of LPD-SiO <sub>2</sub> thin film deposition on b-Si NWs	72
Figure 3.7	Filmetrics F20 Thin Film Analyzer [232].	73
Figure 3.8	Attenuated total reflectance-Fourier-transform infrared (ATR-FTIR) spectrometer [233]	75
Figure 3.9	Flowchart for the fabrication of b-Si NWs and LPD-SiO <sub>2</sub> /b-Si NW-based solar cells.	76
Figure 3.10	Flowchart of b-Si NW-based solar cell fabrication process	76
Figure 3.11	Schematic diagram of the fabrication of b-Si NWs-based solar cell.	79
Figure 3.12	Image and schematic diagram of thermal evaporation system (Edwards Auto 306 model).	80
Figure 3.13	Image and schematic diagram of Hall effect measuring system; Model: LAKESHORE CONTROLLER 601/DRC-93CA (the schematic is adapted from [236]).	81
Figure 3.14	Photograph image showing sample b-Si NWs-based solar cell for Hall effect measurements.	81
Figure 3.15	Photograph image and schematic diagram of LED-based light source solar simulator (model: TMS-2X2 Forter Technology).	82
Figure 3.16	White LED, Compact Fluorescent (CFL) and Incandescent bulbs Spectra. AM1.5G standard solar spectrum is shown for comparison [238]	83
Figure 4.1	Top and oblique (30°) FESEM images of b-Si NWs formed on p-type with different etching times; (a & e) 5 min, (b & f) 10 min, (c & g) 15 min and (d & h) 20 min.	85
Figure 4.2	Cross-sectional view FESEM images of b-Si NWs formed on p-type etched for durations of (a) 5 min, (b) 10 min, (c) 15 min and (d) 20 min.	86
Figure 4.3	AFM images of b-Si NWs on p-type (100) for different etching times (a) 5 min (b) 10 min (c) 15 min (d) 20 min	87
Figure 4.4	Reflection (a) and absorption (b) curve of b-Si nanowires etched at different etching duration of 5 min, 10 min, 15 min and 20 min. Planar c-Si reference is used for comparison	88

Figure 4.5	Length of b-Si NWs (primary y-axis) and corresponding WAR (secondary y-axis) after etching with different etch times	89
Figure 4.6	Top view and cross-sectional view FESEM images of b-Si NWs formed on p-type etched for durations of (a and a') 5 min, (b and b') 10 min, (c and c') 15 min and (d and d') 20 min	90
Figure 4.7	Relationship between the average depth of NWs and their surface coverage against different etching time (5–10 min)	90
Figure 4.8	FESEM cross-sectional images of SiO <sub>2</sub> films deposited by LPD process on planar c-Si at different durations; (a) 20 min, (b) 60 min, (c) 100 min and (d) 140 min	92
Figure 4.9	Top view and oblique (30°) FESEM images of b-Si NWs before and after LPD of SiO <sub>2</sub> films: (a and f) before LPD, (b and g) after 20 min, (c and h) after 60 min, (d and i) after 100 min, and (e and j) after 140 min	93
Figure 4.10	FESEM cross-sectional images of b-Si (a) before LPD and (b), (c), (d) and (e) after LPD of SiO <sub>2</sub> films with increased deposition duration; 20 min, 60 min, 100 min and 140 min	94
Figure 4.11	EDX results of b-Si NWs (a) before LPD-SiO <sub>2</sub> film deposition and (b), (c), (d), and (e) after LPD-SiO <sub>2</sub> film deposition at different deposition times; 20 min, 60 min, 100 min, and 140 min.	95
Figure 4.12	AFM images of b-Si (a) before LPD process and (b), (c), (d), and (e) after LPD process with different durations; 20 min, 60 min, 100 min and 140 min	96
Figure 4.13	(a) Reflection and (b) absorption curves of LPD SiO <sub>2</sub> films on b-Si NWs at different deposition duration: 20 min, 60 min, 100 min, and 140 min. Note that b-Si before the LPD process is included as a reference.	97
Figure 4.14	Relationship between the thickness of SiO <sub>2</sub> , WAR and refractive index with increased LPD duration.	98
Figure 4.15	ATR-FTIR absorption spectra of the LPD-SiO <sub>2</sub> thin films deposited with different solution concentrations of H <sub>3</sub> BO <sub>3</sub> ; 0.04 M, 0.06 M, 0.08 M, and 0.10 M with a fixed 0.02 M H <sub>2</sub> SiF <sub>6</sub> .	99
Figure 4.16	FESEM images of the top view and cross-sectional of b-Si NWs before LPD-SiO <sub>2</sub> film deposition (a and a") and b-Si NWs after LPD-SiO <sub>2</sub> film deposition in 0.1M H <sub>2</sub> SiF <sub>6</sub> solution at different H <sub>3</sub> BO <sub>3</sub> solution concentration, (b and b") 0.04M,	

	(c and c") 0.06M, (d and d") 0.08M and (e and e") 0.1M	100
Figure 4.17	AFM images of b-Si NWs (a) before LPD-SiO <sub>2</sub> film deposition and b-Si NWs after LPD-SiO <sub>2</sub> film deposition in 0.1M H <sub>2</sub> SiF <sub>6</sub> solution at different H <sub>3</sub> BO <sub>3</sub> solution concentrations (b) 0.04M, (c) 0.06M, (d) 0.08M and (e) 0.1M.	102
Figure 4.18	Dependence of deposition rate and RMS film roughness on the added H <sub>3</sub> BO <sub>3</sub> concentration in 0.1 M H <sub>2</sub> SiF <sub>6</sub> solution	102
Figure 4.19	Reflectance curves of LPD-SiO <sub>2</sub> film deposited on b-Si NWs in 0.1M H <sub>2</sub> SiF <sub>6</sub> solution at different H <sub>3</sub> BO <sub>3</sub> solution concentrations; 0.04M, 0.06M, 0.08M and 0.1M with Ref b-Si for comparison.	104
Figure 4.20	FE-SEM images of the top view and cross-sectional of b-Si NWs before LPD-SiO <sub>2</sub> film deposition (a and a") and b-Si NWs after LPD-SiO <sub>2</sub> film deposition in 0.02M H <sub>3</sub> BO <sub>3</sub> solution at different H <sub>2</sub> SiF <sub>6</sub> solution concentration, (b and b") 0.02M, (c and c") 0.04M, (d and d") 0.06M and (e and e") 0.08M.	105
Figure 4.21	AFM images of b-Si NWs (a) before LPD-SiO <sub>2</sub> film deposition and b-Si NWs after LPD-SiO <sub>2</sub> film deposition in 0.02M H <sub>3</sub> BO <sub>3</sub> solution at different H <sub>2</sub> SiF <sub>6</sub> solution concentrations (b) 0.02M, (c) 0.04M, (d) 0.06M and (e) 0.08M.	106
Figure 4.22	Dependence of deposition rate and RMS film roughness on H <sub>2</sub> SiF <sub>6</sub> concentration with the addition of 0.02M H <sub>3</sub> BO <sub>3</sub> solution.	106
Figure 4.23	Reflectance curves of LPD-SiO <sub>2</sub> film deposited on b-Si NWs in 0.02M H <sub>3</sub> BO <sub>3</sub> solution at different H <sub>2</sub> SiF <sub>6</sub> solution concentrations; 0.02M, 0.04M, 0.06M and 0.08M with Ref b-Si for comparison.	108
Figure 4.24	FESEM images of the top view and cross-sectional of b-Si NWs LPD-SiO <sub>2</sub> film deposition in 0.1M H <sub>2</sub> SiF <sub>6</sub> solution with the additional of 0.02M H <sub>3</sub> BO <sub>3</sub> solution at different temperatures (a and a") 30°C, (b and b") 40°C, (c and c") 50°C and (d and d") 60°C.	109
Figure 4.25	EDX results of b-Si NWs LPD-SiO <sub>2</sub> film deposition in 0.1M H <sub>2</sub> SiF <sub>6</sub> solution with the addition of 0.02M H <sub>3</sub> BO <sub>3</sub> solution at different temperatures (a) 30°C, (b) 40°C, (c) 50°C and (d) 60°C.	110
Figure 4.26	AFM images of b-Si NWs LPD-SiO <sub>2</sub> film deposition in 0.1M H <sub>2</sub> SiF <sub>6</sub> solution with the addition of 0.02M H <sub>3</sub> BO <sub>3</sub> solution at	

	different temperatures (a) 30°C, (b) 40°C, (c) 50°C and (d) 60°C.
Figure 4.27	Dependence of deposition rate and RMS film roughness on different deposition temperatures
Figure 4.28	Reflectance curves of LPD-SiO <sub>2</sub> film deposited on b-Si NWs at different temperatures: 30°C, 40°C, 50°C, and 60°C with Ref b-Si for comparison.
Figure 4.29	Schematic diagram of the incident light into the anti-reflective structure of (a) b-Si NWs/Si, (b) conventional ARC of SiO <sub>2</sub> /Si and (c) SiO <sub>2</sub> /b-Si NWs/Si
Figure 4.30	ATR-FTIR spectrum of the LPD-SiO <sub>2</sub> /c-Si and LPD-SiO <sub>2</sub> /b-Si NWs-based solar cells
Figure 4.31	30°-tilted top-view and cross-sectional FESEM images; (a and b) b-Si NWs and (c and d) LPD-SiO <sub>2</sub> /b-Si NWs-based solar cells
Figure 4.32	Core-shell p-n junction structure of specific b-Si NWs after the diffusion process
Figure 4.33	AFM images of (a) c-Si-based solar cell, (b) LPD-SiO <sub>2</sub> /c-Si-based solar cell, (c) b-Si NWs-based solar cell and (d) LPD-SiO <sub>2</sub> /b-Si NWs based solar cell
Figure 4.34	Reflection curves for c-Si (before diffusion), c-Si (after diffusion), LPD SiO <sub>2</sub> /c-Si (after diffusion), b-Si (before diffusion), b-Si (after diffusion) and LPD SiO <sub>2</sub> /b-Si (after diffusion).
Figure 4.35	J-V curves for c-Si and b-Si NWs-based solar cells without LPD-SiO <sub>2</sub> film and c-Si and b-Si NWs-based solar cells coated with LPD-SiO <sub>2</sub> film

### LIST OF SYMBOLS

D Absorber thickness

α Absorption coefficient

E<sub>a</sub> Activation energy

 $S(\lambda)$  AM1.5G solar spectrum

 $E_g \hspace{1cm} Bandgap \\$ 

Φ<sub>SBH</sub> Barrier height

θ Bragg's angle or light incidence angle

V<sub>bi</sub> Built-in potential

P Concentration of etchant

D Crystallite size

J<sub>c</sub> Current density of cathodic process

J<sub>D</sub> Dark current density

Degrees

°C Degree Celsius

 $au_{eff}$  Effective lifetime

 $\eta$  Efficiency

E Electric field

Q Electron

EA Electron affinity

n<sub>e</sub> Electron carrier concentration

μ<sub>e</sub> Electron carrier mobility

N<sub>s</sub> Electron Density

V Electron velocity

eV Electron volt

v Frequency

 $\beta$  Full width at half maximum

R<sub>H</sub> Hall coefficient

V<sub>H</sub> Hall Voltage

n<sub>p</sub> Hole carrier concentration

 $\mu_p$  Hole carrier mobility

N Ideality factor

B Magnetic field

B<sub>z</sub> Magnetic induction

P<sub>max</sub> Maximum power generated

J<sub>sc(max)</sub> Maximum short-circuit-current density

M Moles per litre

N<sub>2</sub> Nitrogen

Z Number of electrons transferred

 $\Omega$  Ohm

V<sub>oc</sub> Open-circuit voltage

C<sub>ox</sub> Oxidant concentration

O Oxygen

% Percentage

hv Photon energy

h Planck's constant

P<sub>in</sub> Power of light photon per area (1000 W/m<sup>2</sup> at standard

conditions)

K<sub>c</sub> Reaction rate constant

n Refractive index

 $R(\lambda)$  Reflection

J<sub>o</sub> Reverse saturation current density

s Second

R<sub>s</sub> Series resistance

R<sub>sheet</sub> Sheet resistance

K Shape constant

J<sub>sc</sub> Short-circuit current density

R<sub>sh</sub> Shunt resistance

d Thin-film thickness

T Transmission

V Volt

 $\lambda$  Wavelength

### LIST OF ABBREVIATIONS

Al<sub>2</sub>O<sub>3</sub> Aluminum oxide

NH<sub>4</sub>OH Ammonium hydroxide

ARC Antireflection coating

AFM Atomic Force Microscope

ALD Atomic Layer Deposition

ATR-FTIR Attenuated Total Reflectance-Fourier Transform Infrared

b-Si Black silicon

b-Si NWs Black silicon nanowires

BSF Back surface field

H<sub>3</sub>BO<sub>3</sub> Boric acid

CdTe Cadmium Telluride

CO<sub>2</sub> Carbon dioxide

CSCs Carrier selective contacts

CVD Chemical Vapour Deposition

CFL Compact Fluorescent

CB Conduction band

CPD Contact potential difference

CIGS Copper Indium Gallium and Selenide

c-Si Crystalline silicon

DI H<sub>2</sub>O Deionized water

DC Direct current

EDX Electron Dispersive X-ray

CH<sub>3</sub>COOH Ethanol

EQE External quantum efficiency

FFC-Cambridge Farthing-Chen-Cambridge

FESEM Field Emission Scanning Electron Microscope

FOM Figure of merit

FF Fill factor

FWHM Full width at half maximum

GaAs Gallium arsenide

Au Gold

HCL Hydrochloric acid

HF Hydrofluoric acid

H<sub>2</sub>O<sub>2</sub> Hydrogen peroxide

H<sub>2</sub>SiF<sub>6</sub> Hydrofluorosilicic acid

a-SiN<sub>x</sub>:H Hydrogenated amorphous silicon nitride

a-Si:H Hydrogenated amorphous silicon

D<sub>it</sub> Interfacial trap densities

IBC Interdigitated back contact

IQE Internal quantum efficiency

LED Light emitting diode

LPD Liquid Phase Deposition

LT Laser texturing

MACE Metal-assisted chemical etching

μA Microampere

μm Micrometer

ml Milliliter

Min Minute

nm Nanometer

NPs Nanoparticles

HNO<sub>3</sub> Nitric acid

(NO<sub>3</sub>) Nitric ions

 $\Omega$  cm Ohm centimeter

PERL Passivated emitter with rear locally diffused

PECVD Plasma Enhanced Chemical Vapor Deposition

PIII Plasma Immersion Ion Implantation

H<sub>3</sub>PO<sub>4</sub> Phosphoric acid

PSG Phosphosilicate glass

PL Photoluminescence

PV Photovoltaic

PVMD Photovoltaics Materials and Devices

KOH Potassium hydroxide

PCE Power conversion efficiency

QFL Quasi-Fermi Level

RCA Radio Corporation of America

RF Radio frequency

RIE Reactive ion etching

RMS Root mean square

SIMS Secondary Ion Mass Spectroscopy

SRH Shockley Read Hall

SiN<sub>x</sub> Silicon nitride

SiO<sub>2</sub> Silicon dioxide

SiO<sub>2</sub>.xH<sub>2</sub>O silicic acid powder

Ag Silver

Ag+ Silver ions

Ag NPs Silver nanoparticles

AgNO<sub>3</sub> Silver nitrate

NaOH Sodium hydroxide

SRP Spreading Resistance Profiling

STCs Standard Test Conditions

SRV Surface recombination velocity

Ta<sub>2</sub>O<sub>5</sub> Tantalum pentoxide

TMAH Tetramethylammonium hydroxide

SnO<sub>2</sub> Tin oxide

TiO<sub>2</sub> Titanium oxide

TMO Transition metal oxide

TCO Transparent conductive oxide

WO<sub>3</sub> Tungsten trioxide

UV-Vis-NIR Ultraviolet-visible near-infrared

VB Valence band

V<sub>2</sub>O<sub>5</sub> Vanadium pentoxide

H<sub>2</sub>O Water

WAR Weighted average reflectance

# PEMPASIFAN PERMUKAAN BERKOS RENDAH UNTUK SEL SURIA HITAM SILIKON OLEH TEKNIK PEMENDAPAN FASA CECAIR

#### **ABSTRAK**

Black silicon (b-Si) ialah struktur permukaan yang terbaik untuk sel suria kerana pemantulan jalur lebar yang rendah dan sifat penangkapan cahaya yang unggul dalam kawasan panjang gelombang 300-1100 nm. Dalam proses fabrikasi b-Si, goresan kimia berbantukan logam tanpa elektrik satu langkah (MACE) dijalankan bagi menghasilkan wayar nano (NW) dengan ketinggian kira-kira 0.4 – 0.8 μm membentuk pantulan jalur lebar yang rendah tetapi membawa kepada penggabungan semula permukaan yang tinggi dalam sel suria b-Si. Untuk menangani isu ini, pempasifan permukaan yang cekap adalah tidak dapat dielakkan, penting untuk membangunkan sel suria b-Si berkecekapan tinggi. Pempasifan permukaan dengan pembentukan silikon dioksida terma (SiO<sub>2</sub>) adalah kaedah konvensional yang melibatkan pemprosesan suhu tinggi. Suhu proses yang tinggi boleh mempengaruhi b-Si bertekstur nano, menjejaskan penyerapan jalur lebar cahaya dalam sel suria. Oleh itu, pemendapan fasa cecair (LPD) adalah permukaan alternatif teknik pempasifan menangani isu penggabungan semula permukaan. Proses LPD adalah mudah, melibatkan persediaan mudah, murah, penggunaan suhu pemprosesan yang rendah, kadar pemendapan tinggi dan serasi dengan pemendapan kawasan yang besar, dijalankan pada suhu bilik. Kajian ini menyelidik filem nipis LPD-SiO<sub>2</sub> pada b-Si. Filem licin SiO<sub>2</sub> telah ditumbuhkan pada b-Si NW daripada larutan asid hidrofluorosilisik (H<sub>2</sub>SiF<sub>6</sub>) 0.1M dengan asid borik (H<sub>3</sub>BO<sub>3</sub>) 0.02 M Keputusan morfologi permukaan mendedahkan bahawa ketebalan filem SiO<sub>2</sub> meningkat daripada 10.2 kepada 35.2 nm dengan peningkatan masa pemendapan. Kebergantungan struktur

mikro filem nipis LPD-SiO2 pada parameter kepekatan larutan, suhu pemendapan, kadar pemendapan dan kekasaran filem juga telah diperiksa. Pantulan purata wajaran (WAR) dipengaruhi oleh ketebalan filem nipis LPD-SiO2; apabila ketebalan filem meningkat, WAR berkurangan untuk panjang gelombang antara 300 hingga 1100 nm disebabkan, oleh kesan penggredan indeks biasan b-Si NWs. Untuk sel suria berasaskan b-Si, b-Si mengurangkan WAR daripada 36.8% untuk (c-Si) kepada 12.9% dalam kawasan panjang gelombang 300-1100 nm. Dengan 30 nm SiO2 didepositkan pada b-Si, WAR berkurang lagi kepada 10.7%. Sifat elektrik yang lebih baik telah dicerminkan dalam ketumpatan arus litar pintas ( $J_{sc}$ ) dipertingkatkan 22.7 mA/cm², voltan litar terbuka ( $V_{oc}$ ) 488.5 mV dan faktor isian (FF) 38% selepas pempasifan SiO2. Kecekapan penukaran ( $\eta$ ) bagi sel suria b-Si telah meningkat daripada 8.0% untuk sel yang tidak dipasifkan kepada 9.6% untuk sel yang dipasifkan. Oleh itu, filem pempasifan LPD-SiO2 sangat sesuai untuk meningkatkan sifat sel suria b-Si.

# LOW-COST SURFACE PASSIVATION FOR BLACK SILICON SOLAR CELLS BY LIQUID PHASE DEPOSITION TECHNIQUES

#### **ABSTRACT**

Black silicon (b-Si) is a promising surface structure for solar cells due to its low broadband reflectance and superior light trapping properties within the 300–1100 nm wavelength region. For the fabrication of b-Si, one-step electroless metal-assisted chemical etching (MACE) is employed which produces nanowires (NWs) with heights of about  $0.4 - 0.8 \mu m$  that result in low broadband reflectance but leads to high surface recombination in b-Si solar cells. To address this issue, efficient surface passivation is inevitable, which is essential for developing high-efficiency b-Si solar cells. Surface passivation by the formation of thermal silicon dioxide (SiO<sub>2</sub>) is the conventional method that involves high-temperature processing. The high process temperatures could deteriorate the nanotextured b-Si formed by the etching process, compromising broadband light absorption in the solar cells. Therefore, liquid phase deposition (LPD) is a promising alternative surface passivation technique that can reduce the surface recombination issue. The LPD process is facile, involves a simple setup, is inexpensive, has a low processing temperature, is capable of a high deposition rate, compatible with a large area deposition, and is carried out at room temperature. This work investigates the LPD of SiO<sub>2</sub> thin films on b-Si. Smooth SiO<sub>2</sub> films are grown on b-Si NWs from a 0.1 M hydrofluorosilicic acid (H<sub>2</sub>SiF<sub>6</sub>) solution with 0.04 M boric acid (H<sub>3</sub>BO<sub>3</sub>). The surface morphological results reveal that the thickness of SiO<sub>2</sub> film increases from 10.2 to 35.2 nm with increased deposition time. The dependence of the microstructure of LPD-SiO<sub>2</sub> thin films on the solution concentration parameters, deposition temperature, deposition rate and film roughness are also examined. The weighted average reflection (WAR) is impacted by the thickness of the LPD-SiO<sub>2</sub> thin film; as the film thickness increases, the WAR decreases for wavelengths ranging from 300 to 1100 nm, owing to the refractive index grading effect by the b-Si NWs. For the b-Si based solar cells, the b-Si reduces WAR from 36.8% for (c-Si) to 12.9% within the wavelength region of 300–1100 nm. With 30 nm of SiO<sub>2</sub> deposited on the b-Si, the WAR reduces further to 10.7%. The improved electrical properties have been reflected in enhanced short-circuit current density ( $J_{sc}$ ) of 22.7 mA/cm<sup>2</sup>, open-circuit voltage ( $V_{oc}$ ) of 488.5 mV and fill factor (FF) of 38% after the SiO<sub>2</sub> passivation. The corresponding power conversion efficiency ( $\eta$ ) of the b-Si solar cell increases from 8.0% for the unpassivated cell to 9.6% for the passivated cell. Thus, the LPD-SiO<sub>2</sub> passivation film is highly favourable for improving the properties of b-Si solar cells.

### **CHAPTER 1**

### INTRODUCTION

### 1.1 Introduction

Global energy consumption is constantly increasing, causing a rapid reduction of fossil fuel sources, which remain the dominant energy source for many emerging countries. Using fossil fuels to generate energy has resulted in negative environmental consequences such as global warming (climate change). Solar energy has sparked widespread interest as a potential alternative and has advanced rapidly in the previous decade [1]. Currently, fossil fuels such as oil and coal account for 80% of worldwide energy consumption, directly linked to widespread water and air pollution and climate change via greenhouse gas emissions [2]. Due to population and economic growth, they are rendering fossil fuels insufficient to meet future energy demands. Other sustainable alternative energy technologies, such as wind, solar, geothermal, biodiesel, and biomass energy sources, are being investigated to meet the growing energy demand [3]. Solar energy has emerged as one of the most promising renewable energy sources in recent decades, with the potential to be widely investigated and adopted to meet the ever-increasing demand for energy [4],[5].

Unlike every pure and ecologically friendly energy source, solar energy is not constrained by systems performance, topographic boundaries, or low technical possibilities such as ecological and land-use restrictions. Solar energy is the world's most important source of renewable energy and harnessing the sun's power is the key potential for sustainable energy. Solar energy is the world's principal renewable energy source and harnessing the sun's influence can be the key to long-term energy sustainability. Photovoltaics (PV) is one of the world's leading renewable sources of

electricity production. Electricity accounted for 17% of global final energy consumption in 2010 and accounted for 43% in 2050 [6]. PV is expected to meet approximately 25% of the global electricity demand by 2050 (Figure 1.1(a)). Total installed PV capacity is expected to grow from 384 GW in 2017 to 8,519 GW in 2050 (Figure 1.1(b)) [7].

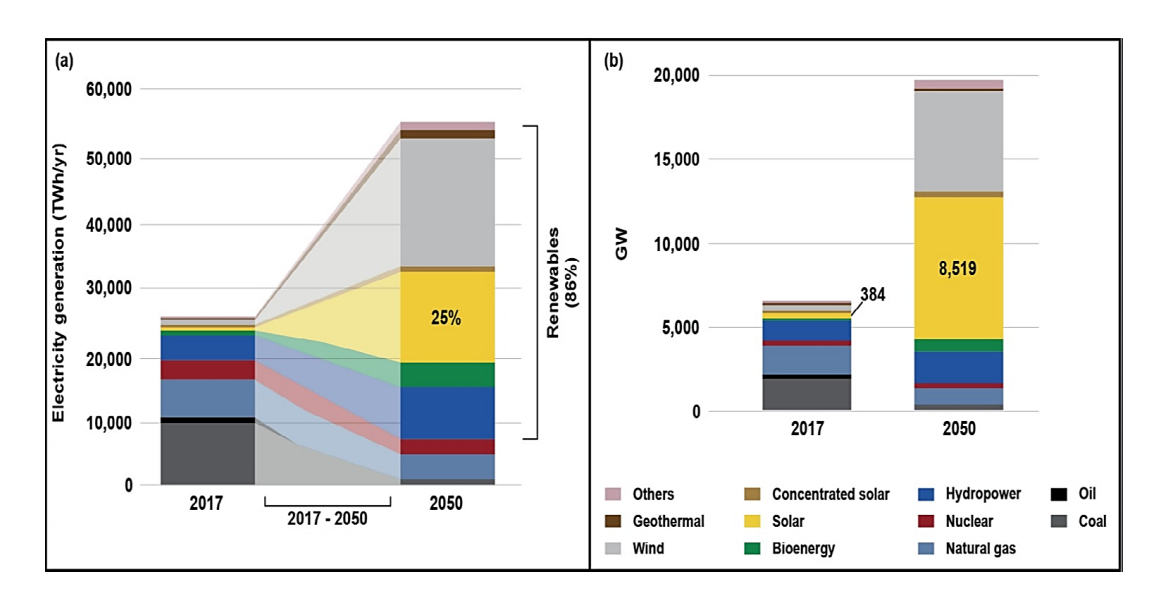


Figure 1.1 (a) Global electricity generation from renewables and fossil fuels until 2050 and (b) Global installed capacity by energy source (adapted from IRENA's Global Renewables Outlook, 2020) [6].

Since the introduction of advanced PV devices in 1973, the cost of PV technology has dropped from \$500 per watt to less than \$1 per watt. PV has become a \$100 billion sector despite pandemic-related impacts, with global PV installations increasing by 32.6% from 144 GW in 2020 to 191 GW in 2021 [8-10]. The grid parity parameter can be used to determine whether the price of solar energy can contend with the costs of conventional electricity [11]. This parameter may be affected by (i) innovations in PV technology, (ii) simplification/optimization of production processes, (iii) more excellent implementation and (iv) use of less expensive materials. In the PV industry, two breakthroughs occurred, allowing this technology to be adopted. Imposition of the Back surface field (BSF) solar cell was the first

breakthrough that resulted in a significant reduction in recombination losses [12]. The second is a silicon nitride  $(SiN_x)$  film formed by plasma-enhanced chemical vapour deposition (PECVD) and chemical vapour deposition (CVD). It functions as an anti-reflective coating (ARC) and improves light absorption in the bulk silicon [13],[14].

PV technologies are classified into wafer-based PV (also known as 1<sup>st</sup> generation PV) and thin-film cell PV (2<sup>nd</sup> generation PV). Crystalline silicon (c-Si) cells (both mono and multi-crystalline silicon) and gallium arsenide (GaAs) cells fall into the first category. Because of their mature technology, c-Si solar cells have dominated the PV market and account for more than 90% of total production [15],[16]. Whereas thin-film PV like cadmium telluride (CdTe), and copper (Cu) indium (In) gallium (Ga) selenide (Se<sub>2</sub>) (CIGS) are notorious for inexpensive production process [17], [18]. Organic PV, such as dye-sensitized solar cells, have the same advantage [19], [20]. C-Si solar cells require nearly 100 times the amount of material as thin-film solar cell. Even though terawatt solar power is a significant issue, conversion efficiency is another value factor that directly influences the cost per W<sub>p</sub> of c-Si-based solar cells.

C-Si currently dominates the PV market, accounting for more than 90% of total output, as shown in Figure 1.2 [21]. In 1941, Russell Ohl [22] discovered the properties of c-Si and the concept of c-Si-based PV devices, following the first PV discovery by French physicist Alexandre-Edmond Becquerel in 1839 [23]. Later that year, in 1954, G.L. Pearson, Daryl Chapin, and Calvin Fuller developed the first c- Si solar cell at Bell Laboratories in New Jersey, demonstrating the solar energy conversion to electricity on c-Si p-n junctions [24]. The developed solar cells could produce power at 60 watts per square metre of the c-Si surface, equating to about 6% efficiency [24]. Since then, there has been a surge in interest in producing solar cells made from c-Si.

The best commercially available c-Si modules now achieve 24.4% efficiency, and manufacturers such as Kaneka aims for even higher efficiency by 2030 [25].

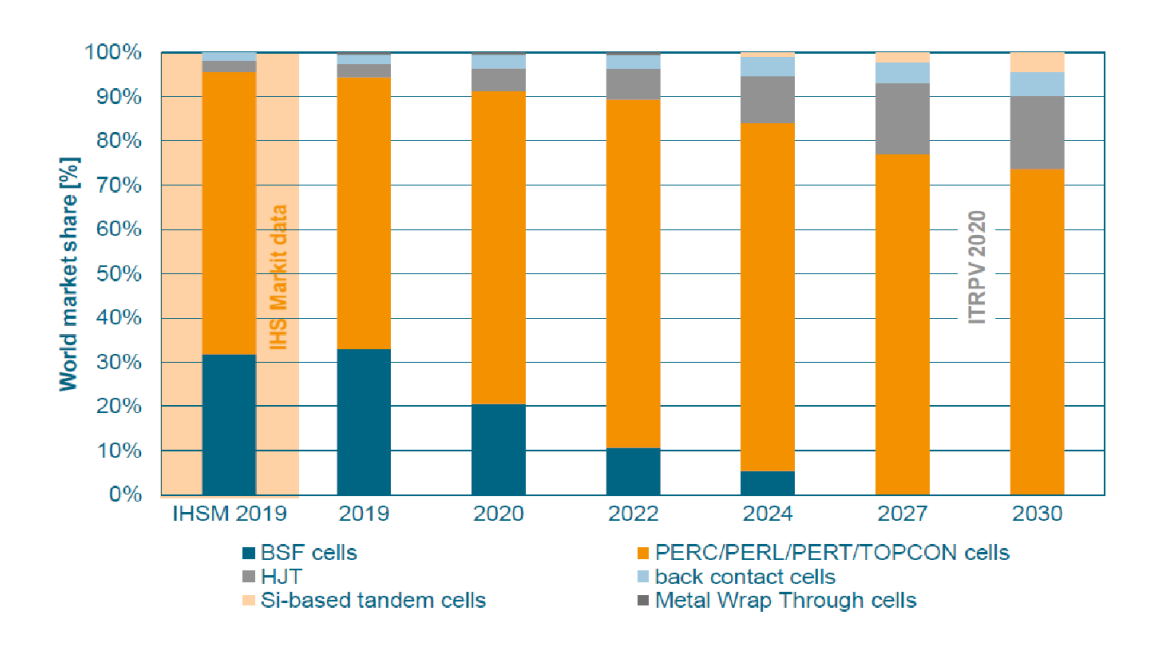


Figure 1.2 World market share for different c-Si solar cell technologies and extrapolation of demand to the Year 2030. Source: ITRPV 2020 [21].

From the late 1970s to the late 1980s, more than 20% of efficient c-Si and GaAs solar cells were already reported (as shown in Figure 1.3). Solar cells that can convert up to 46% of solar energy into electricity using various techniques are being developed. If the linear trend shown in Figure 1.3 continues, a power conversion efficiency (PCE) greater than 40% under standard test conditions (STCs) can be achieved by the end of 2021. Electrical losses must be minimised to achieve high PCE while increasing the amount of incident light that can be efficiently absorbed in active absorbent materials by suppressing the surface reflection. This can be accomplished by increasing light scattering on the absorbing surface or decreasing the discontinuity refractive index distance trapped between the absorbing surface and nearby air medium [26]. Similarly, this can be accomplished by collecting large-angle illuminated incident light [26].

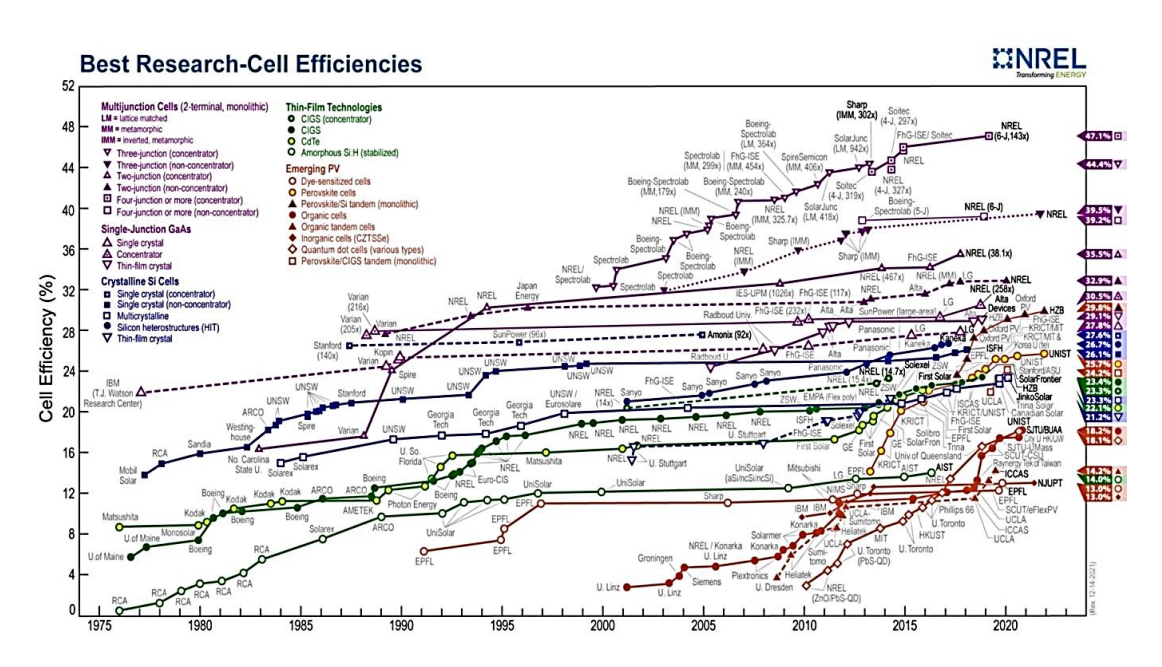


Figure 1.3 National renewable energy laboratory (NREL) solar cell efficiency chart [27].

The dominance of c-Si is due to the abundance of sand (silica, SiO<sub>2</sub>), technological maturity, non-toxicity and high market share [28]. Furthermore, its improved conversion efficiency (expected to be about 26 % by late 2020) and reduced technology costs are another factors. Despite the superiority and high market share of c-Si solar cells in the PV industry, inadequate light absorption owing to the indirect bandgap and low absorption factor of c-Si is still an important issue [28]. The c-Si absorber's poor light absorption is owing to a high-level reflectance of incident photons (approximately 35-40%) in the wavelength range of 300-1100 nm [29], [30]. C-Si absorber material can reduce the broadband reflection either by increasing light dispersion on the c-Si's surface or by decreasing the refractive index discontinuity distance between the c-Si absorber surface and surrounds [31-34].

One of the most promising, highly-efficient-silicon-based PV technologies is black silicon (b-Si) for solar cells. B-Si is a c-Si wafer which comprises micro/nano textures with excellent broadband light absorption from the ultraviolet (UV) down to infrared (IR) regions of the electromagnetic (EM) spectrum [35-37]. Due to

nanotextures on the surface of the c-Si wafer, the wideband reflection suppresses the c-Si wafer (planar) from 40% to around 10% of b-Si within the wavelength region of 300–1100 nm. This suppression is accomplished by the impact of refractive index (n) grading, in which the array of nanotextures at the surface of the c-Si wafer behaves as a graded-index multi-layer anti-reflective coating (ARC) [38]. Nanotextures are perceived by the incident light as a medium with a refractive index amongst air medium (n = 1.0) and the bulk c-Si (n = 3.8) [39], [40]. The b-Si experiences a progressive increase in the refractive index because of incident light travelling through it, which leads to the suppression of broadband reflection. This suppression of broadband reflection in the b-Si resulted in improved broadband light absorption [41]. The etching and texturization processes of the c-Si wafer are essential and must be optimised to create high-efficiency b-Si solar cells. However, surface modification and texturization lead to increased dangling bonds, resulting in more significant surface recombination or reduced carrier lifetime.

Numerous techniques have been developed for the fabrication of b-Si, such as reactive ion etching (RIE), laser texturing (LT), metal-assisted chemical etching (MACE), as well as plasma immersion ion implantation (PIII) [42], [43-45]. The non-large-scale manufacturing of RIE, PIII, and LT-based b-Si for solar cells is attributable to the need for high-technology equipments and faster processing techniques that might result in b-Si solar cells at quite a high rate per unit watt (\$/W). Among these techniques, MACE remains the most facile, cost-efficient, and compatible with large-scale fabrication [46]. The MACE technique does not really necessitate the use of high-tech equipments or time-consuming procedures for processing. Silver (Ag), gold (Au), and copper (Cu) are the most widely used catalysts for MACE. The b-Si-based solar cells manufactured with b-Si developed using Au and Cu-based metal catalysts endure high

recombination losses [47], [48]. The Au or Cu metal traces, which act as recombination locations in the solar cells, are the source of the high recombination. This work selects Ag metal as a catalyst to achieve lower recombination losses in b-Si-based solar cells.

Surface recombination in c-Si solar cells can reduce cell efficiency significantly. Surface passivation, which is applying a thin film to the b-Si surface, is one of the most common methods of reducing the surface recombination. The ability of the thin film to passivate is based on two distinct effects: chemical passivation and field-effect passivation. Chemical passivation is about reducing dangling bonds. On the other hand, field-effect passivation is based on the charge in the thin film, which drives electrons or holes far and prevents their recombination on the surface, depending on the charge polarity. A few thin films utilized for surface passivation can indeed serve a dual purpose: they can act as an anti-reflection coating (ARC) and minimize reflective losses at the same time.

The doping density and type of passivated surface, or the polarity of permanent charge, influence the potential application of various thin films. Furthermore, the thin film must not reflect the incident photons in the wavelength range important for solar cell performance. Thermal silicon dioxide (SiO<sub>2</sub>) and plasma-enhanced chemical vapour deposition (PECVD) hydrogenated amorphous silicon nitride (a-SiN<sub>x</sub>:H), and hydrogenated amorphous silicon (a-Si:H) are conventional materials for surface passivation of silicon solar cells [49-51]. However, alternative atomic layer deposited (ALD) aluminium oxide (Al<sub>2</sub>O<sub>3</sub>) thin film has attracted increasing interest as a promising surface passivation material recently [52-54].

However, the MACE texture continues to be non-optimized from an optical standpoint because the nanostructures are often smoothed to permit higher

conformality and thus more effective surface passivation. The reflectivity of MACE-textured wafers with no ARC remains high, like 15–30%, owing to the smoothening [55]. Thermally grown SiO<sub>2</sub> has been shown to passivate the surfaces of MACE structures with a reduced 5% reflectivity [56], [57]. Even though thermal SiO<sub>2</sub> is growing conformally on nanostructures, the passivation efficiency is restricted because of the thin film's lower density of static charges [58-60]. Furthermore, metal contamination is increased by high-temperature oxidation following the MACE process.

Although low reflectance has been achieved with the mix of micro/nano textures and ARC, there is still potential for advancement, notably because solar radiation comprises various wavelengths and does not continually appear on the solar cell surface perpendicularly. B-Si (nanocones, nanopyramids, nanograss, and so on) has been intensively researched for its capability to lower reflectance throughout a broad spectral range and tolerance angle. However, placing b-Si on the front surface of solar cells has consistently resulted in a compromise: the benefit from low reflectance is oppressed by the increased surface recombination caused by the nanostructure's high surface area. Conventional thermal oxidation surface passivation materials have not yet offered adequate surface passivation for b-Si, owing to low conformality or inadequate field-effect [61] as well as high temperatures. As a result, issues concerning b-Si surface recombination have gone unaddressed.

### 1.2 Problem statement

Although c-Si solar cells possess high percentage in the PV market, c-Si (planar) light absorption is inadequate due to the high surface reflectance (35-40%) of incident light in the wavelength range of 300-1100 nm. It has become a big problem

for solar cells. Because of its high surface reflectance, c-Si only absorbs between 60% and 65% of the incident light. The high surface reflectance of c-Si can be reduced by the b-Si absorber and is described as a method to improve the performance of c-Si solar cells [62]. Apart from the other methods of reducing reflectance mentioned above, there are other methods such as laser irradiation that is used to bombard a Si surface to generate nanostructures and method involves collective oscillations of free electrons in NPs to excite localized surface plasmon resonance.

Currently, b-Si nanowires (NWs) can be produced with the MACE process. But the present MACE process involves a protracted process, starting from a couple of minutes to a few hours, producing b-Si NWs with a length of 1-6 μm [26], [63-70]. Such lengthy nanotextures show higher surface recombination because of the higher nanotexture aspect ratio, resulting in low PCE in the b-Si solar cells [47], [66-71]. Besides, lengthy procedures for processing are irrelevant to industrial scalability. Therefore, optimising the fabrication process to obtain c-Si-optimized b-Si nanotextures with shorter lengths (less than 1 μm) using a shorter process time. Additionally, the developed b-Si should also have a low broadband reflectance in the wavelength range of 300–1100 nm in order not to affect the J<sub>sc</sub> of the b-Si NW solar cells. Therefore, the development of the b-Si is described as using a shorter process period and having low wideband reflectance within the 300–1100 nm wavelength range.

The only effective way to overcome the greater surface recombination rate produced by long NWs flowing through b-Si NW solar cells is to shorten the NWs or passivate the b-Si surface with thin coatings of SiO<sub>2</sub>, Al<sub>2</sub>O<sub>3</sub>, or titanium dioxide (TiO<sub>2</sub>) [72-77], which is essential for developing high-efficiency b-Si NWs solar cells. Numerous studies have been conducted to achieve highly efficient c-Si-based solar

cells by utilising SiO<sub>2</sub> on various surfaces, such as planar c-Si, microtextured c-Si, and inverted cone textured c-Si [78]. Because the gaps among the NWs on the b-Si surface are difficult to cover with the conventional passivation layer growth method, thermal oxidation (SiO<sub>2</sub>) was proposed as an effective passivation technique to address this issue because oxygen can reach the surface of the b-Si NWs at any point during the thermal oxidation process. Nevertheless, thermal SiO<sub>2</sub> deposition is a standard method for depositing SiO<sub>2</sub> on these surfaces [79], [80]. The thermal SiO<sub>2</sub> process involves high-temperature processing, which degrades the nanotextured b-Si, reducing broadband light absorption in the solar cells. Thus, a low-temperature and facile surface passivation technique is highly desired for high-efficiency b-Si NWs-based solar cells [81],[82].

In this work, the liquid phase deposition (LPD) technique is investigated, which has the distinctive benefits of being low-cost, low processing temperature, high deposition rate, compatible for large area deposition, and involves a simple setup. The LPD process is carried out at room temperature with the solution of fluorosilicic acid (H<sub>2</sub>SiF<sub>6</sub>), silicic powder (SiO<sub>2</sub>.xH<sub>2</sub>O) and deionized water (DI H<sub>2</sub>O). This work aims to optimize the MACE process for producing b-Si NWs and create room temperature SiO<sub>2</sub>-based LPD to decrease surface recombination in b-Si NWs solar cells, improving the PCE.

### 1.3 Objectives

Objectives of this work are as the following:

To optimize etching time (within 5 to 20 minutes) using one-step
 MACE process to produce b-Si.

- 2. To develop and characterise a room temperature LPD-SiO<sub>2</sub> process to reduce surface recombination in b-Si NW solar cells.
- To investigate the effects of LPD-SiO<sub>2</sub> surface passivation on the performance of b-Si NW solar cells in comparison to the solar cell without passivation.

### 1.4 Thesis outline

This work is divided into 5 chapters.

**Chapter 1** discusses the general introductory background of solar energy and the rationales for exploring b-Si nanotextured solar cells. The chapter likewise presents the significance of surface passivation, problem statement, and objectives.

**Chapter 2** includes an overview of the relevant theoretical background and the literature on which the work is based. And also describes the background theories and principles of b-Si characteristics for solar cells applications, surface passivation, and the LPD process.

Chapter 3 contains a comprehensive account of the method and materials used in this project. This involves the practical fabrication processes of the b-Si NWs and the deposition of SiO<sub>2</sub> thin film by the LPD process. This chapter also discusses the fabrication and characterization of devices in the NOR laboratory used to study the properties of b-Si-NW surfaces.

**Chapter 4** presents the outcomes of b-Si NWs of the one-step MACE process, including the impact of the process parameters on the b-Si structure. The improvement in absorption accomplished on the textured surfaces of b-Si NWs compared to the planar c-Si reference material is investigated and discussed. The best surface

passivation schemes are presented using LPD-SiO<sub>2</sub> on c-Si (planar) and b-Si NWs surfaces. Furthermore, this chapter describes the optical morphological, and electrical properties of the b-Si NWs and the LPD-SiO<sub>2</sub>/b-Si NWs.

**Chapter 5** concludes the entire work and summarizes the actual outcomes and contributions to the knowledge of the b-Si. This chapter, furthermore, outlines the recommendations for further work.

#### **CHAPTER 2**

#### THEORETICAL BACKGROUND AND LITERATURE REVIEW

#### 2.1 Introduction

The chapter presents the theoretical background to the operation of solar cells, black silicon solar cells, the refractive index grading effect, and surface recombination. This chapter also discusses the literature on b-Si for its application in solar cells. Furthermore, the chapter reviews various works reporting b-Si fabrication based on RIE, LT, PIII, MACE, and the fundamental processes of the LPD techniques for surface passivation.

## 2.2 Solar radiation

The sun is a natural energy supply that transmits electromagnetic radiation with wavelengths ranging from 250 to 2500 nm. Figure 2.1 illustrates that the flux density of electromagnetic radiation varies with wavelength. The whole of this spectrum signifies the wavelength-weighted worth of solar radiation beyond the atmosphere (1,387 W/m² or AM0) [83]. Still, owing to the absorption and scattering of light by atmospheric clouds, air molecules, dust, oxygen, smog, and CO<sub>2</sub>, this level of radiation at sea level on a bright day is less than about 1000 W/m² on the earth's surface (AM1.5) [83]. In general, the irradiance at the earth's surface is determined by the path length of light as it travels through the atmosphere, which is also determined by the angle of incidence of the light. Equation (2.1) shows this using the representative air mass (AM) parameter [84].

$$AM = \frac{1}{\cos \theta} \tag{2.1}$$

In Equation (2.1),  $\theta$  is the light's angle relative to the zenith, defined as a point perpendicular to the earth's surface. The worldwide standard spectrum for characterising solar cells has been described as an air mass of 1.5, consisting of diffuse and direct radiation. The spectrum is AM1.5G. If PV measurements are carried out using this spectrum at 25° C below 1000 W/m², then the PV response of the device is comparable to others and scaled globally. AM1 refers to the vertical incidence of the sun at sea level at the equator. AM0 is the spectrum beyond the atmosphere. Both are shown in Figure 2.1.

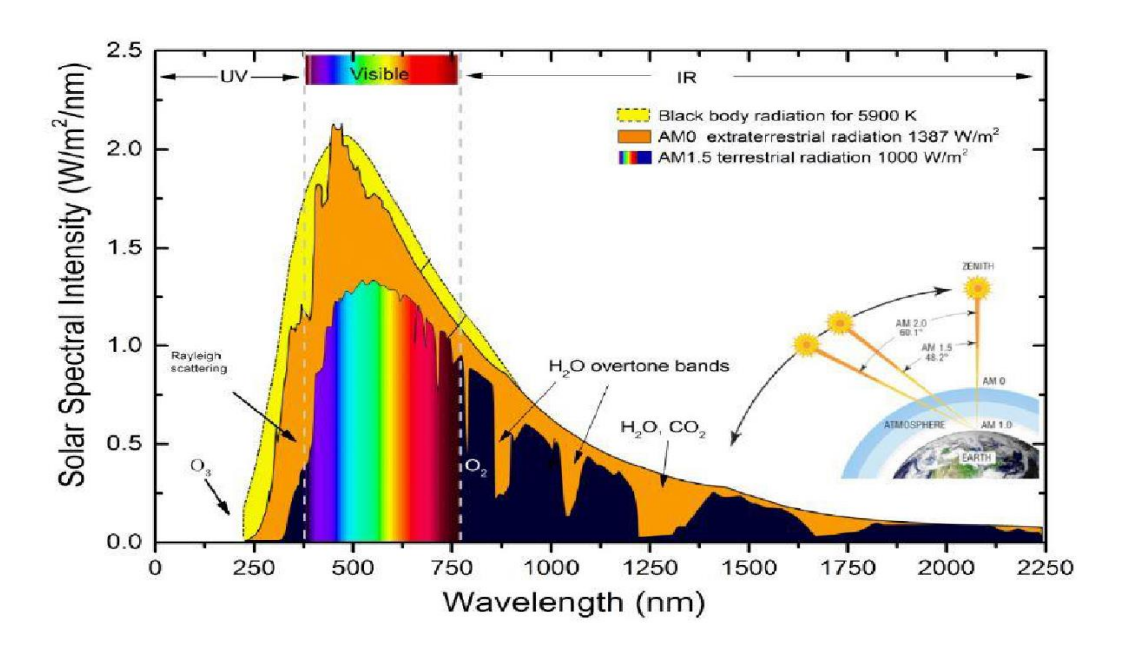


Figure 2.1 AM1.5G standard solar spectrum (spectral irradiance as a function of wavelength), direct part of AM0 spectrum of AM1.5G spectrum. The data are available from the original NREL data file [85] and the embedded image (for AM 0, AM 1 and AM 1.5) was taken from the Newport company website [86].

### 2.3 Silicon solar cells

When the incident light hits the surface of the c-Si, it experiences three scenarios: reflection, transmission, or absorption. Equation (2.2) mathematically defines photon energy [87]. **h** is Planck's constant,  $\mathbf{v}$  the frequency of the photon,  $\mathbf{c}$  the speed of light and  $\boldsymbol{\lambda}$  the wavelength of the incident photon in Equation (2.2).

$$E = hv = \frac{hc}{\lambda} \tag{2.2}$$

Following the French physicist Alexander Edmond Becquerel's discovery of the PV effect, Planck and Einstein reported Equation (2.2) for the first time. The PV effect is also based on Equation (2.2). However, in order to better realize the PV effect and how solar cells work, it is necessary to comprehend the fundamentals underlying the transformation of optical energy to electrical energy in the c-Si. First, this concept necessitates a minimum two-level system, as illustrated in Figure 2.2 (a-c). This system allows electrons to transition from low to high energy levels as they absorb light [88]. According to the solid-state band theory, the bulk semiconductor c-Si absorber possesses about 10<sup>22</sup> atoms/cm<sup>3</sup>, and specific energy levels forming a continuous energy band (Figure 2.2 (d)). The valence band's energy level is the lowest, and the conduction band's energy level is the highest. The bandgap is the amount of space between these bands. Under normal circumstances (absolute zero point), electrons cannot leave this bandgap [88]. An incident photon must give up its energy to an electron in order to excite it from the valence band into the conduction band. Figure 2.2 (e) depicts how electrons move from the valence band to the conduction band in direct bandgap materials such as GaAs. However, electron excitation in indirect bandgap materials such as c-Si (Figure 2.2(f)) is supplied by vibrations of the crystal lattice (phonon) [89]. Equation (2.13) states that 1.12 eV E<sub>g</sub> of c-Si equals infrared radiation, suggesting that the c-Si-based solar cells can generate a significant amount of electricity using only visible light and near-infrared radiation. Therefore, when the c-Si absorber absorbs the incident light, its energy is transformed into electrochemical potential and electrical energy by generating electron-hole pairs.

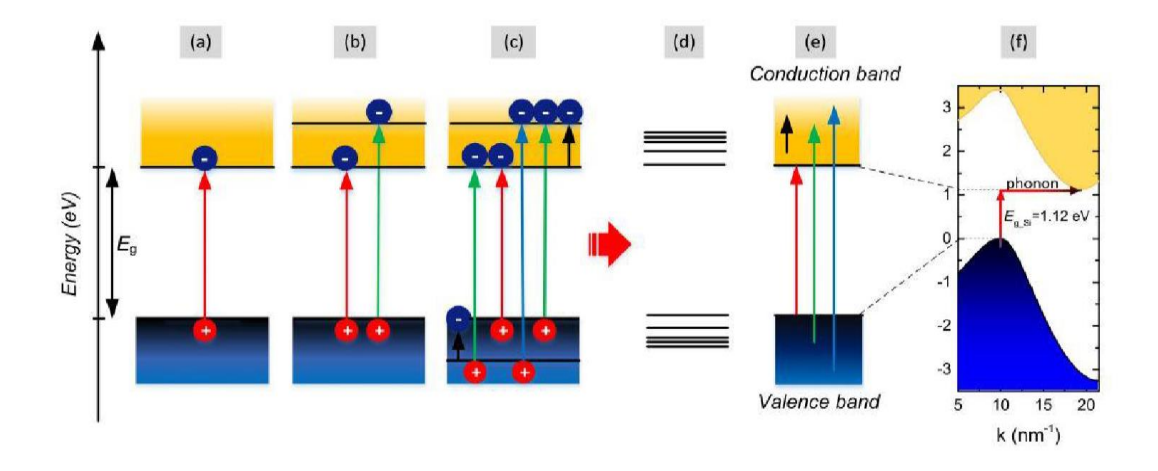


Figure 2.2 Two-level system showing photon absorption only at a certain energy level (wavelength) (a-e) with an increasing number of energy levels (horizontal) for direct bandgap material like GaAs. The colour of the arrows represents the colour of the absorbed light, while (f) is the band structure of c-Si (indirect bandgap material). (Taken from [89]).

Carrier annihilation (recombination) occurs when energy quanta are generated since pairs of carriers (electrons and holes) have opposite polarities. As a result, the solar cell's primary function effectively avoids recombination while also efficiently directing electron-hole pairs to the charging terminals. The maximum short-circuit current density ( $J_{sc\ (max)}$ ) of a solar cell determines the ability to separate the generated electron-hole pairs effectively.  $J_{sc\ (max)}$  is the integral of the photons falling on c-Si in the wavelength range of 300 to 1100 nm specified by Equation (2.3). Equation (2.3) is effective barely when individual absorbed photon stimulates an electron, and all the stimulated electrons are directed to the metal contacts for collection and extraction. If each absorbed photon excites an electron, EQE = IQE x (1-R-T), about 1-R due to the opacity of c-Si [67],[90].

$$J_{SC(max)} = q \int_{300 \text{ nm}}^{1100 \text{ nm}} EQE(\lambda) . S(\lambda) d\lambda$$
 (2.3)

In Equation (2.3),  $\bf q$  is the charge on the electron and  $\bf S(\lambda)$  is the standard solar photon spectral density for the AM1.5G solar spectrum. The  $\bf J_{sc~(max)}$  attainable by a c-Si solar cell is about 43.5 mA/cm<sup>2</sup> (i.e., when the c-Si solar cell absorbs about  $10^{17}$ 

photons/cm/sec) [89]. For the calculation, the c-Si solar cell is assumed to have unity carrier collection (i.e., IQE=1).

# 2.3.1 Operating principle

Once p-type c-Si and n-type c-Si are intercalated, free electrons diffuse into the p-type region through the n-type region. Electron flow produces positively charged pentavalent dopant impurity ions in the "depletion region," which is the boundary region between the n-type and p-type edges. Within the p-type side, holes begin to diffuse into the n-type region, putting behind negatively charged trivalent dopant impurity ions. At the junction between n-type c-Si and p-type c-Si materials, set-up ions of the dopant impurities built an electric field. The presence of the "built-in" electric field affects free electrons and holes. The holes are attracted to the negative trivalent dopant ions, while the electrons are attracted to the positive pentavalent dopant ions. This means that the "built-in" electric field causes certain electrons and holes to stream toward the diffusion-generated flow (Figure 2.3). The fundamental basis for operating solar cells is based on the "built-in" electric field [88], [89].

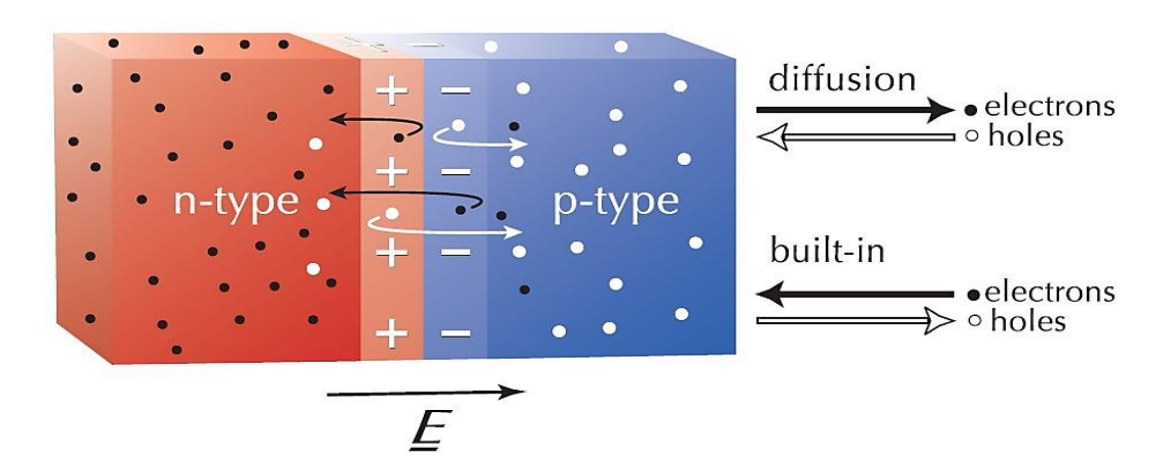


Figure 2.3 Schematic of p-n junction showing the motion of mobile electrons and holes due to diffusion and the "built-in" electric field [88].

Due to the presence of a "built-in" electric field, current and voltage can be induced at the intercalated p-n junction when photons strike it. The induced current and voltage are caused by the excitation of electrons to a higher energy state by the incident photon (or an externally applied voltage). Because some bonds in the crystal structure have been broken, electrons are free to move. Assume that the "built-in" electric field effectively differentiates the free carriers; the current flows through the junction towards the flow stream of the holes. If the electrons and holes remain in the solar cell before being collected, they will recombine, resulting in an insufficient response [88],[89].

When the two differently doped parts are isolated, the quasi-Fermi level (QFL) can be determined using Equations (2.4) and (2.5), as shown in Figure 2.4(a). When the two parts come into contact, the system achieves a thermal equilibrium, and the energy levels are illustrated in Figure 2.4(b).

$$E_{Fn} = E_c + K_b T \ln \left( \frac{N_D}{N_C} \right)$$
 (2.4)

$$E_{Fp} = E_v + K_b T ln \left(\frac{N_A}{N_V}\right)$$
 (2.5)

Where  $N_D$  and  $N_A$  are the donor and acceptor concentrations, and  $N_C$  and  $N_V$  are the conduction and valence band states' effective densities,  $E_c$  and  $E_v$  are the undoped band energies of the conduction and valence bands, respectively,  $K_b$  is the Boltzmann constant, and T is the temperature,  $E_{Fn}$  and  $E_{Fp}$  are QFL of electrons and holes.

The built-in potential  $(V_{bi})$ , also known as diffusion voltage, is the polarisation achieved at the junction (see Equation (2.6)).

$$V_{bi} = \frac{K_B T}{q} \ln \left( \frac{N_A N_D}{n_i^2} \right)$$
 (2.6)

In the dark state (and thus in thermal equilibrium), the electric field levels out the concentration gradient at the junction, and the Fermi level is constant throughout the device. This level is divided into two as a result of photon absorption (illumination) according to Equation (2.7):

$$E_{Fn} - E_{Fp} = K_B T ln \left( \frac{n_p p_p}{n_i^2} \right)$$
 (2.7)

Where  $n_p$  is the concentration of electrons (minority carriers),  $p_p$  is the concentration of holes (majority carriers) and  $n_i$  is the intrinsic charge carrier density.

The electrochemical potential gradient created by the difference between the two levels, along with the device, is the primary steering factor for charge separation.

Electrodes produce contact with surfaces in real devices to collect separated charge carriers and generate electrical energy. At the surfaces, majority carriers typically recombine with diffuse minority carriers, leaving no energy accessible for harvesting. But the recombination rate is sufficiently high, the Fermi levels at the two terminals may finally achieve the same energy. Carrier-selective layers are employed on contacts to reduce this behaviour. A strongly doped region with p<sup>+</sup> for holes and n<sup>+</sup> for electrons is the simplest carrier-selective layer. The p<sup>+</sup> and n<sup>+</sup> regions have the energetic impact of pinning the bands at the two terminals, as seen in Figure 2.4c. Because recombination is partially suppressed, the Fermi level differs at the two terminals [89].

Thus, in order to power collection is then necessary to enhance contact selectivity; in the case of heavily doped regions this condition applies (Equation (2.8)):

$$N_{A,p} + N_{D,n} + \ge n_p p_p \approx \Delta_n (N_A + \Delta_n)$$
 (2.8)

Where  $\Delta_n$  is the electron excess carrier concentration.

Under this condition, the bias in the absorber is equal to the Fermi Levels splitting at the electrodes. Writes the following as in Equation (2.9):

$$V_{bi} \ge \frac{E_{Fn} - E_{Fp}}{q} \approx \frac{K_B T}{q} \ln \left( \frac{\Delta_n (N_A + \Delta_n)}{n_i^2} \right)$$
 (2.9)

It is also possible to refer to the level of the splitting in the absorber as the implied open-circuit voltage ( $iV_{oc}$ ).

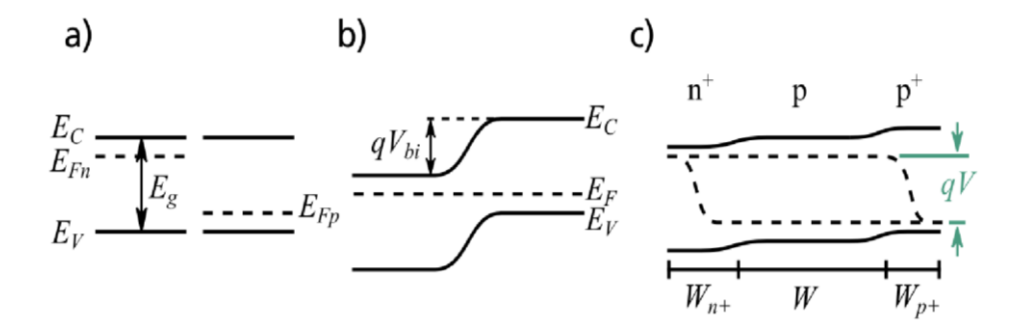


Figure 2.4 Fermi levels of a) n-doped and p-doped semiconductors alone, b) a p-n homojunction in thermal equilibrium and c) an ideal  $n^+|p|p^+$  device upon illumination [89].

## 2.3.2 Solar cell efficiency parameters

This device can be modelled using the structure shown below to understand the functions of solar cell parameters better.

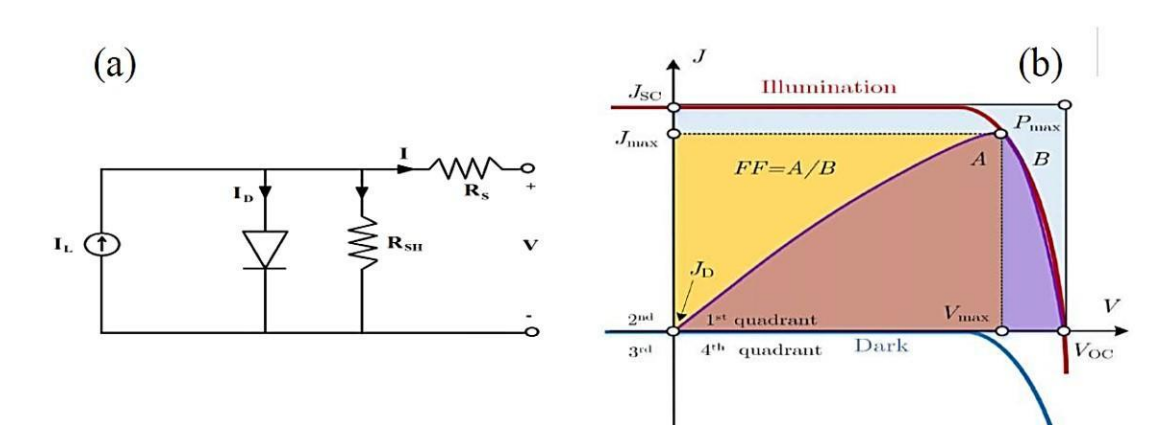


Figure 2.5 (a) Electrical circuit of a solar cell showing generated photon current in parallel with p-n-junction diode and a shunt resistor, and in series with another resistor and (b) current density-voltage characteristic curves of solar cell under illumination and in the dark (adopted from [29]).

The solar cells' electrical equivalent circuit diagram is shown in Figure 2.5. Figure 2.5 also shows the current density-voltage behaviour of the solar cell under light and dark conditions, indicating that  $J_{sc}$  is zero in the dark (i.e.,  $J(V) = -J_D$ ). The Shockley diode Equation (2.10) describes the current flowing over the p-n junction diode in Figure 2.5: (a). When the diode lights up, a photocurrent is created opposite to the diode current. Under illumination, the photocurrent is generated in the opposite direction as the diode current. This gives rise to the Shockley diode Equation (Equation (2.11); assuming the two-diode model if the diode is not ideal) under illumination as provided and discussed using Equation (2.12).

Equations (2.10) and (2.11) can also be stated in the form of current density instead of current by substituting J for I.

$$I_{D} = I_{O} \left\{ \exp \left( \frac{qV}{nKT} \right) - 1 \right\} \tag{2.10}$$

$$I_{D} = I_{L} - I_{O} \left\{ exp \left( \frac{qV}{nKT} \right) - 1 \right\}$$
 (2.11)

 $I_D$  denotes the current flowing through the diode,  $I_O$  the reverse saturation current, q the elementary charge, V is the voltage across the diode and shunt resistor, n is the ideality factor, K the Boltzmann's constant, and T the absolute temperature. Generally, the solar cell current is represented by Equation (2.12), which combines the series resistance ( $R_S$ ) and shunt resistance ( $R_{sh}$ ) (Equation (2.12)), where V is substituted by  $V + R_s I$  because the current and series resistance contributes to the voltage across the diode in addition to the terminal voltage.

$$I_{D} = I_{L} - I_{O} \left\{ exp\left(\frac{q(V+R_{S}I)}{nKT}\right) - 1 \right\} - \frac{V+R_{S}I}{R_{Sh}}$$
 (2.12)

Equation (2.12) is a transcendence equation for which there is no universal analytic solution V or I. The equation demonstrates that to optimise c-Si-based solar cell performance (output power), the I and V across terminals needs to be maximised. In the same way that  $I_0$  needs to be minimised,  $R_s$  needs to be minimised at the same time  $R_{sh}$  needs to be maximised.

The total current density of the c-Si solar cell is provided by Equation (2.13)

$$J(V) = J_{SC} - J_{D} (2.13)$$

 $J_{sc}$  is the short circuit current density, which is the maximum solar cell current when the voltage across the solar cell is zero.  $J_D$  is the solar cell's voltage-dependent recombination current density.

The maximum V accessible from a solar cell with no current flow (J=0) is known as the open-circuit voltage ( $V_{oc}$ ). Since Equation (2.14) is obtained by employing Equation (2.16), the  $V_{oc}$  can be calculated.

$$V_{oc} = \frac{nKT}{q} \ln \left( \frac{J_{sc}}{J_D} + 1 \right)$$
 (2.14)

The fill factor (FF) is the squaring of a solar cell's J-V curve. The ratio of the maximum power generated by the solar cell to the product of  $V_{oc}$  and  $J_{sc}$  is defined as FF. The FF is defined by the area A/B in Figure 2.5(b) and expressed mathematically in Equation (2.15).

$$FF = \frac{P_{\text{max}}}{J_{\text{sc}}V_{\text{oc}}} = \frac{J_{\text{max}}V_{\text{max}}}{J_{\text{sc}}V_{\text{oc}}}$$
(2.15)

 $P_{max}$  is the maximum power supplied by the solar cell (which is zero in both states,  $V_{oc}$  and  $J_{sc}$ ) at the point of maximum power, defined as the product of current and voltage from the IV curve in Figure 2.5 (b).

The efficiency  $(\eta)$  of a c-Si solar cell is the ratio between the  $P_{max}$  produced by the solar cell and the incident light power and is expressed mathematically in Equation (2.16).

$$\eta = \frac{P_{\text{max}}}{P_{\text{in}}} = \frac{FFJ_{\text{sc}}V_{\text{oc}}}{P_{\text{in}}}$$
 (2.16)

The  $P_{in}$  represents the photon power of the incident light, which is usually about 1000  $W/m^2$  under normal circumstances, as shown above.

#### 2.4 Black silicon solar cells

By providing near-ideal diffuse reflectance across the entire c-Si solar spectrum, an array of vertically aligned needle-shaped c-Si structures can lower the amount of specular reflectivity required for high efficiency. The formation of a needle-like layer with properties near or equal to the wavelength of light is used to analyse near-zero specular reflectance over a range of incidence angles, eliminating the need for traditional surface-textured structures and anti-reflective coatings [91]. Suppose the size of the surface features is less than the wavelength of the incident light. In that case, the needle-like nanostructures and microstructures provide beneficial light trapping, which increases the effective optical pathlength in the c-Si solar cells [92]. The size of the b-Si structures is set by the geometry of texture and has a direct influence on the reflectance of the solar cell.

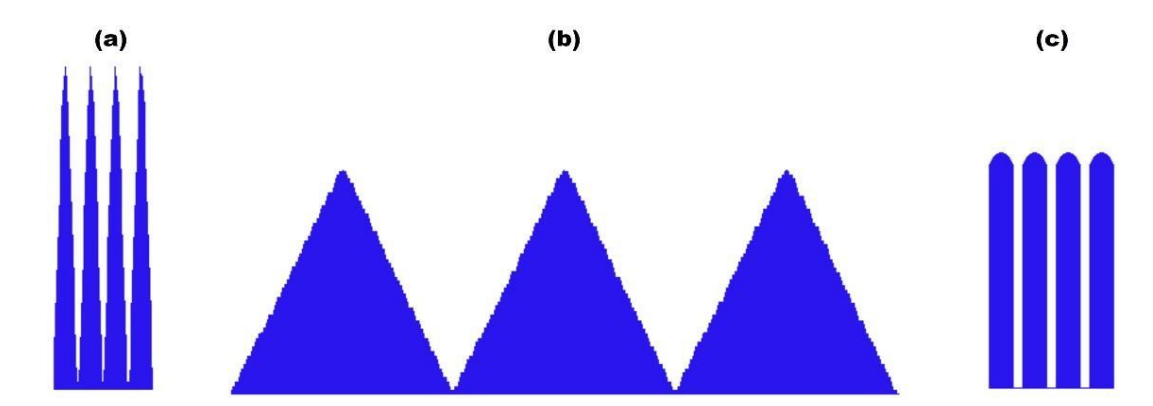


Figure 2.6 (a) Needle-like shape, (b) pyramid shape, and (c) cylinder shape c-Si structures [93].

Figure 2.6 depicts three basic structural forms of b-Si for solar cell applications: needle-like, pyramidal, and cylindrical. As long as the visible light reflectance is kept exceptionally low, c-Si nanostructures in b-Si solar cells could be etched into various shapes. The three b-Si textures shown in the figure above are distributed evenly on the solar cell surface; however, in experiments, the b-Si structures are generally distributed randomly over the c-Si surface for most etching processes [43]. Pyramidal c-Si structures are generally fabricated on a 5-15 μm deep for light scattering and anti-reflection applications [36]. The needle and cylinder-shaped structures in b-Si solar cells are produced in the diameter range of 40-100 nm. Due to the geometry of the three forms of the c-Si structure, the aspect ratios (i.e. ratio of height to width) of the pyramidal structures are smaller than those of the needle-like and cylindrical structures [65].

The most common surface-textured structures for solar cell applications are pyramidal c-Si structures. Due to the size and geometry of the pyramidal structures, pyramidal c-Si structures exhibit the highest surface reflectance of the three basic shapes. Cylindrical c-Si structures have the highest manufacturing requirements. Each cylindrical structure must be etched with high precision to form vertical sidewalls. The use of cylindrical structures has the benefit of being able to be designed to reflect